ORGANIC CHEMISTRY FRONTIERS

RESEARCH ARTICLE

View Article Online
View Journal | View Issue

Cite this: *Org. Chem. Front.*, 2023, **10**, 3219

S,N-Heteropentacene-based molecular donor–acceptor dyads: structure–property relationships and application in single-material organic solar cells†‡

Teresa Kraus, Anna Aubele and Peter Bäuerle *

Received 31st March 2023,
Accepted 16th May 2023

DOI: 10.1039/d3qo00465a

rsc.li/frontiers-organic

Functionalized *S,N*-heteropentacenes SN5′ were used as central donor units in molecular donor–acceptor dyads and were covalently linked to fullerenic acceptor units *via* flexible linkers. Systematically varied structural motifs and characterization of their optoelectronic properties resulted in structure–property relationships and allowed for their application in solution-processed single-material organic solar cells, in which power conversion efficiencies of up to 2.8% were achieved.

Introduction

S,N-Heteroacenes represent an important class of π-conjugated oligomers and comprise planar, ladder-type structures with highly delocalized π-electrons.[1] Functionalization allows for the tuning of their optoelectronic properties and their application as photoactive organic semiconductors in organic solar cells (OSC)[2] or as hole transport materials in perovskite solar cells.[3] In particular, *S,N*-heteropentacenes SN5 and SN5′ with the heteroatom sequence *SNSNS* and *SSNSS*, respectively, were successfully used as donor (D) building blocks in acceptor (A)-terminated so-called ADA-systems, which emerged as efficient photoactive components in either vacuum-processed[4] or solution-processed biphasic bulk-heterojunction solar cells (BHJSC).[5]

In contrast to this common cell architecture, which very recently reached power conversion efficiency (PCE) of 19%,[6] but normally requires tedious multi-parameter optimization and may lack thermodynamic stability, single-material organic solar cells (SMOSC) came into focus again and are currently experiencing a 'renaissance'.[7] Because in comparison to the common biphasic or ternary BHJSCs only one sole photoactive material has to be processed and high long-term stabilities were achieved,[8] SMOSCs are considered attractive candidates for an eased technical production of large-scale organic solar cells.[9] PCEs of >13% have indeed very recently been reported for conjugated D–A block copolymers as photoactive materials[10] and >13% for so-called "double cable" polymers,[11] which represent structurally very complex and polydisperse, less defined systems. Even though molecular D–A dyads and triads reached >5%[12] and with respect to PCE stay somewhat behind the polymers, they are structurally defined and represent reproducible systems.

In this respect, we recently described a series of ambipolar molecular oligothiophene-fullerene D–A dyads (named **dyads 1–10**),[13] which in general contain the well-known and smaller *S,N*-heteroacene dithienopyrrol (DTP) as the core and are covalently linked to fullerenic phenyl-C61/C71-butyric acid (PCBA) acceptors *via* the DTP-nitrogen in a "T-shape" fashion. Various structural parameters have been varied, including variation of the length and type of alkyl ester spacers controlling the precise distance between D and A, replacement of the C_{61}-fullerenic acceptor with the corresponding C_{71}-derivative, and finally variation of the terminal acceptor units in the ADA-type donor part by increasing their acceptor strength. In the frame of this structural concept, 'champion' **dyad 4** shows the so far best photovoltaic performance reaching a PCE of 5.3% and exhibiting excellent long-term stability retaining >95% of the initial performance after one month of continuous illumination and operation (Fig. 1).[12]

In continuation of our work on *S,N*-heteroacenes and their application in organic solar cells, we now report the structural extension in the core donor moiety of molecular D–A dyads by introducing the *S,N*-heteropentacene SN5′ core, which replaces DTP in dyads **D11–D18**. The structural motifs were systematically varied and their consequences on thermal, optical, redox, and photovoltaic properties in SMOSCs were investigated leading to valuable structure–property relationships and insight into device performances.

Institute of Organic Chemistry II and Advanced Materials, University of Ulm, Albert-Einstein-Allee 11, 89081 Ulm, Germany. E-mail: peter.baeuerle@uni-ulm.de

† Dedicated to Prof. K. Meerholz (University of Cologne) on the occasion of his 60th birthday.

‡ Electronic supplementary information (ESI) available. See DOI: https://doi.org/10.1039/d3qo00465a

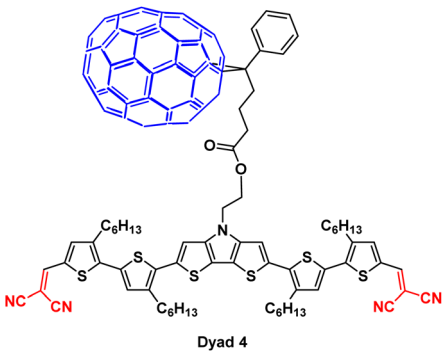

Fig. 1 Structure of molecular oligothiophene-$PC_{71}BM$ dyad **4**.

Results and discussion

Structural variations in dyads D11–D18

We have recently demonstrated that the implementation of ADA-type functionalized heteropentacene SN5′ as donor material in biphasic BJHSCs combined with fullerene acceptors gave PCEs of up to 5.5%.[14] Thereby, in comparison to DTP-based materials and BHJSCs thereof,[15] solar cells based on the extended SN5′-core donor unit showed higher open circuit voltages (V_{OC}) resulting from a larger band gap due to the lower lying highest occupied molecular orbitals (HOMO).[14] Consistently, in the first approach, molecular dyads **D11–D13** were synthesized in which the central hexyl-substituted SN5′-core was functionalized with acceptors of different acceptor strengths: dicyanovinylene (DCV), 1,3-indandione (Ind), and 5,6-dichloro-1,3-indandione (Cl_2-Ind) to yield the ADA-type donor part of the dyads. These were connected to fullerenic acid $PC_{61}BA$ as an acceptor *via* an ethyl ester linker. In order to increase solubility, ethylhexyl (EtHex) side chains were inserted at the β-positions of the SN5′-core to deliver DCV-terminated dyad **D14**. In the second series of D–A dyads, the linker between the D and A subunits was elongated to a hexyl ester moiety in dyads **D15** and **D16**. Moreover, the elongation of the central SN5′ π-system with one thiophene unit at each side leading to dyads **D17** and **D18** should broaden the absorption region. It is expected that the various structural variations have distinct influences on the physical properties of the resulting molecular D–A dyads which are summarized in Scheme 1. Their synthesis and characterization are described in the following, whereby reference compounds **R11–R18** without the pending fullerene subunit were synthesized as well for comparison (see the ESI, ‡).

Synthesis of donor–acceptor dyads D11–D18

Synthesis of SN5′ donor–acceptor dyads D11–D13. The synthetic route to SN5′-dyads **D11–D13** is outlined in Schemes 2 and 3. First, triisopropylsilyl (TIPS)-protected monoethanolamine **2**[16] was reacted with dihexyl-bithienothiophene **1**[17] in a Pd-catalyzed Buchwald–Hartwig amination reaction. The intramolecular ring closure to the fused central pyrrole ring gave *N*-functionalized SN5′-heteroacene **3** in 92% yield which was subsequently formylated with *n*-butyl lithium (*n*-BuLi) and *N*-formylpiperidine (*N*-Fpip) to the corresponding dialdehyde **4** in 74% yield. Deprotection of the TIPS group was achieved under acidic conditions in tetrahydrofuran (THF), and alcohol **5** was isolated in 81% yield. In the next step, Steglich esterification of **5** with fullerene phenyl-C_{61}-butyric acid ($PC_{61}BA$) efficiently resulted in the precursor D–A system **6** (86% yield) (Scheme 2).

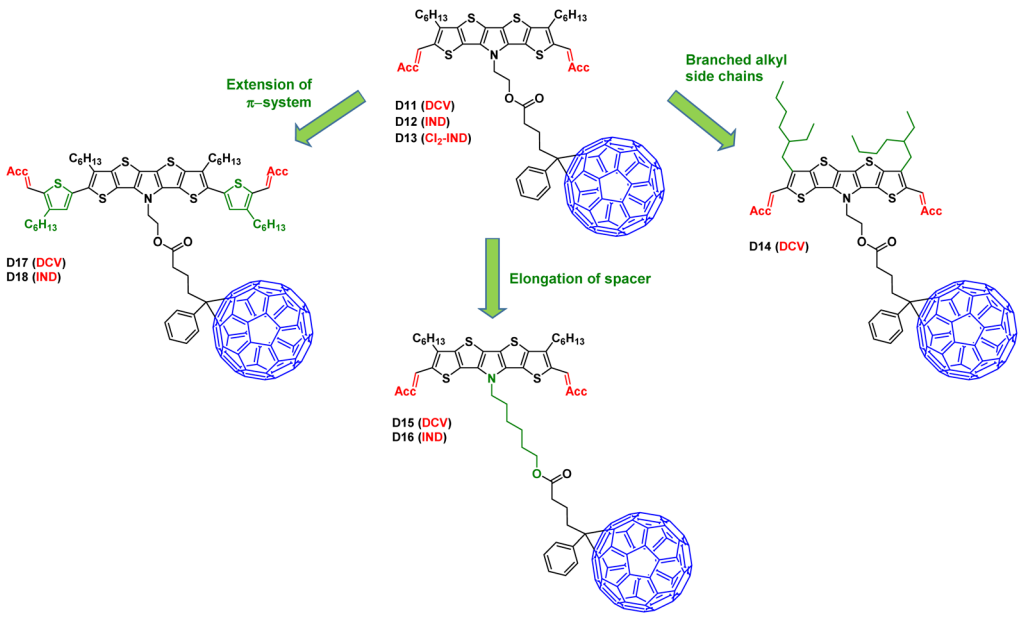

Scheme 1 Concept of structural variations in molecular D–A dyads **D11–D18**, in which the *S,N*-heteropentacene SN5′ core replaces the DTP-based oligothiophene backbone in the previous dyads **D1–D4**.

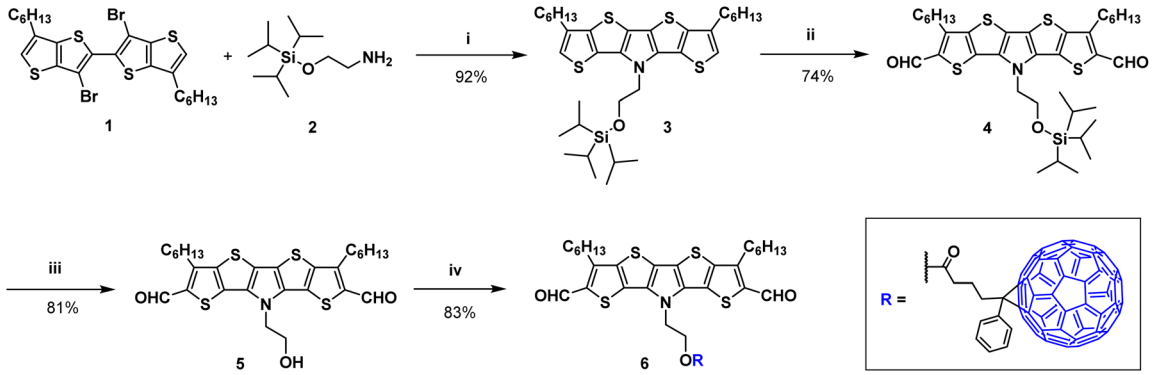

Scheme 2 Synthesis route to SN5′-based D–A intermediate **6**: (i) $Pd(dba)_2$, dppf, NaO^tBu, toluene, 110 °C, 24 h; (ii) *n*-BuLi, *N*-Fpip, THF, −78 °C, rt, 24 h; (iii) THF/HCl (30%), 60 °C, 5.5 h; (iv) $PC_{61}BA$, EDC·HCl, DMAP, CS_2/CB (1 : 2), TEA, 5 d, 40 °C.

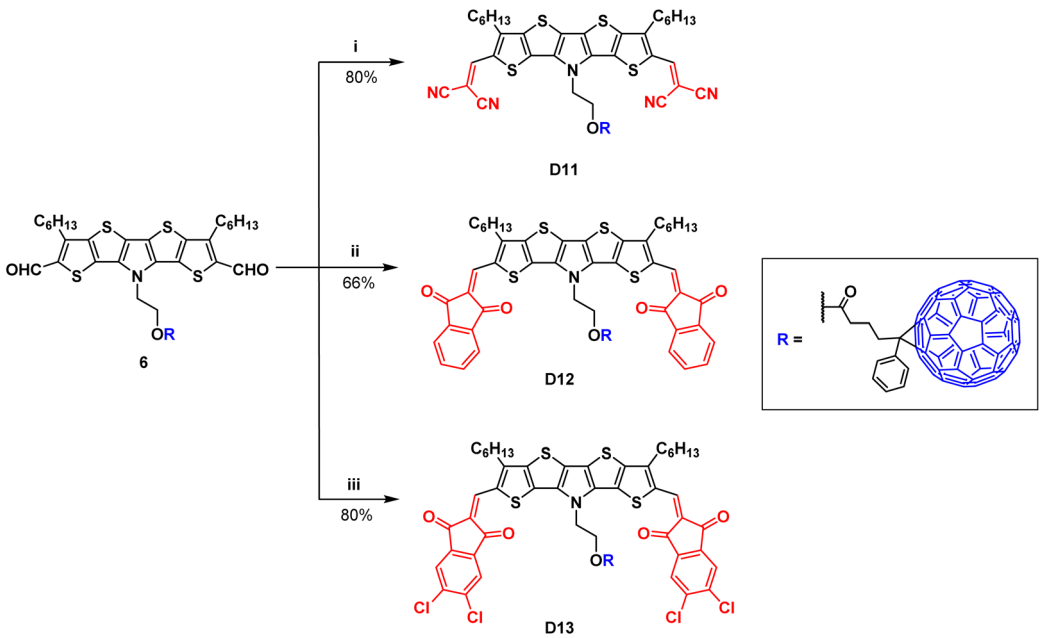

Scheme 3 Synthesis of SN5′-based D–A dyads **D11–D13**: (i) DCV, DCE, NH_4OAc, 70 °C, 5 d; (ii) Ind, DCE, piperidine, rt, 2 d; (iii) Cl_2-Ind, $CHCl_3$, pyridine, 70 °C, 3 d.

The targeted D–A dyads **D11–D13** were obtained by Knoevenagel condensation reactions of intermediate dialdehyde **6** with various acceptors to extend the SN5′ π-system to the favorable ADA configuration. Thus, condensation of **6** with dicyanovinylene (DCV) and ammonium acetate gave **D11** in 80% yield. Insertion of 1,3-indandione (Ind) as the terminal acceptor with piperidine as the base at first led to a product mixture of dyad **D12** and a triply reacted dyad, which was separated by column chromatography. Pure **D12** was then obtained in 66% yield. The reaction of precursor **6** with the strongest acceptor unit, 5,6-dichloroindene-1,3-dione (Cl_2-Ind), delivered D–A **D13** in 80% yield (Scheme 3).

Synthesis of alkylated donor–acceptor SN5′-dyad D14. Branched EtHex side chains were introduced at the outer β-positions of the preceding bithienothiophene in order to increase solubility in general. Synthesis was very similar to that of hexyl derivative **1** and thus 3,4-dibromothiophene **7** was reacted in Friedel–Crafts acylation with EtHex carbonyl chloride **8**[18] using aluminum trichloride ($AlCl_3$) as a Lewis acid. Acylated thiophene **9** was isolated in 84% yield before it was used in a Bradsher ring-closure reaction with ethyl mercaptoacetate and cesium carbonate in DMF. Subsequently, thienothiophene **10** was isolated in 51% yield, which was somewhat lower than that of hexyl derivative **1** probably due to the steric hindrance of the branched alkyl chains. In the next step, the ester functionality was hydrolyzed under basic conditions to give carbonic acid **11** in 79% yield. The following decarboxylation was performed with copper powder in quinoline at high temperatures to obtain thienothiophene **12** in 74% yield. In the last step, thienothiophene **12** was selectively

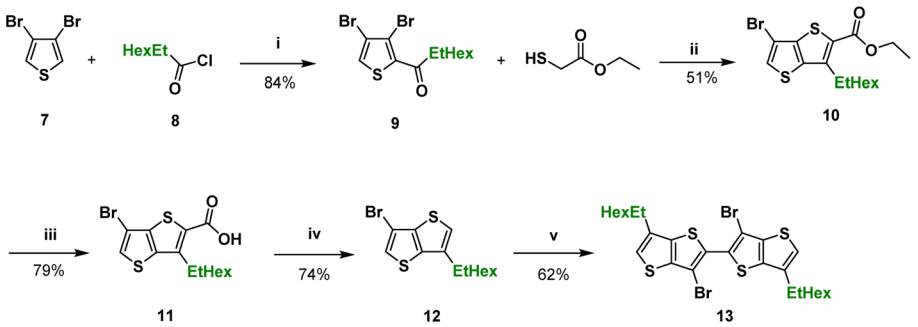

Scheme 4 Synthesis of bithienothiophene **13** bearing ethylhexyl (EtHex) side chains: (i) $AlCl_3$, DCM, 0 °C, 4 h; (ii) Cs_2CO_3, DMF, 70 °C, 7 d; (iii) 1. LiOH, THF, MeOH, reflux, 23 h, 2. HCl (konz.); (iv) Cu, quinoline, 230 °C, 3.5 h; (v) LDA, THF, $CuCl_2$, 22 h, 0 °C–rt.

lithiated with lithium diisopropyl amide (LDA) at the α-position adjacent to the bromo substituent and oxidatively homo-coupled with Cu(II) chloride to give targeted bithienothiophene **13** in 62% yield (Scheme 4).

EtHex-bithienothiophene **13** served as the starting material for the preparation of EtHex-substituted **D14** and was reacted with TIPS-protected ethanolamine **2** in Pd-catalyzed Buchwald–Hartwig amination to give the intermediate SN5′ derivative **14** in 96% yield. The subsequent Vilsmeier–Haack formylation of **14** resulted not only in the targeted introduction of terminal aldehyde groups but also in the removal of the TIPS group. Therefore, alcohol **15** was isolated in only moderate 40% yield, because chloroethyl derivative **16** was formed as the main product (60% yield). Other formylation procedures such as lithiation of **14** with *n*-BuLi and quenching with *N*-Fpip as before resulted only in low yields due to tedious purification. In the next step, SN5′-alcohol **15** was esterified with fullerenic acid $PC_{61}BA$ to the desired D–A dialdehyde **17** in 59% yield. Finally, the terminal DCV-acceptor groups were inserted by Knoevenagel condensation of **17** with malononitrile and **D14** was obtained in 58% yield (Scheme 5).

Synthesis of donor–acceptor SN5′-dyads D15 and D16 comprising a hexyl ester spacer. The synthetic route to **D15** and **D16** is shown in Scheme 6. In Pd-catalyzed Buchwald–Hartwig amination, TIPS-protected hexanolamine **18**[19] was reacted with bithienothiophene **1** to TIPS-protected SN5′-derivative **19**. The subsequent formylation with the *n*-BuLi and *N*-Fpip system delivered dialdehyde **20** in a moderate 32% yield. Hence, as an alternative, SN5′ **19** was first brominated with NBS in chloroform to dibromide **21** (81%), which was then lithiated with *n*-BuLi and quenched with *N*-Fpip to give dialdehyde **20** in higher 49% yield. Acidic deprotection of the TIPS group with HCl in THF led to hexanol **22** (54%), which was esterified with $PC_{61}BA$ under Steglich conditions to give ester **23** (46%). The targeted **D15** was obtained by Knoevenagel condensation of **23** with malononitrile and ammonium acetate (57%), whereby **D16** was obtained in 41% yield by the reaction of **23** with Ind and piperidine.

Synthesis of donor–acceptor dyads D17 and D18 with an extended π-system. The synthetic route to SN5′-dyads **D17** and **D18** with an extended donor π-system included the Pd-catalyzed direct heteroarylation reaction of TIPS-protected SN5′-precursor **3** and iodothiophene aldehyde **24**[20] with potassium acetate as a base. After heating the reaction mixture for 17 hours, the evolved product was precipitated from methanol and purified *via* column and size exclusion chromatography to obtain the elongated dialdehyde **25** in 69% yield. Deprotection of **25** with tetrabutylammonium fluoride (TBAF) delivered alcohol **26** in a quantitative yield which was subsequently esterified with $PC_{61}BA$ under Steglich conditions to deliver the

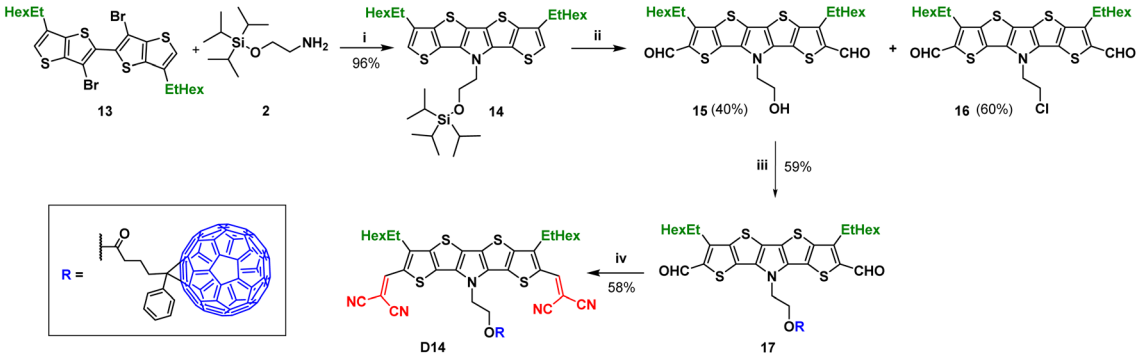

Scheme 5 Synthesis of SN5′-based D–A dyad **D14**: (i) $Pd(dba)_2$, dppf, NaO^tBu, toluene, 110 °C, 24 h; (ii) 1. DMF, $POCl_3$, DCM, reflux, 18 h, 2. $NaOH_{(aq)}$, rt, 1 d; (iii) $PC_{61}BA$, EDC·HCl, CS_2/CB (1 : 2), DMAP, 40 °C, 7 d; (iv) malononitrile, NH_4OAc, DCE, 80 °C, 22 h.

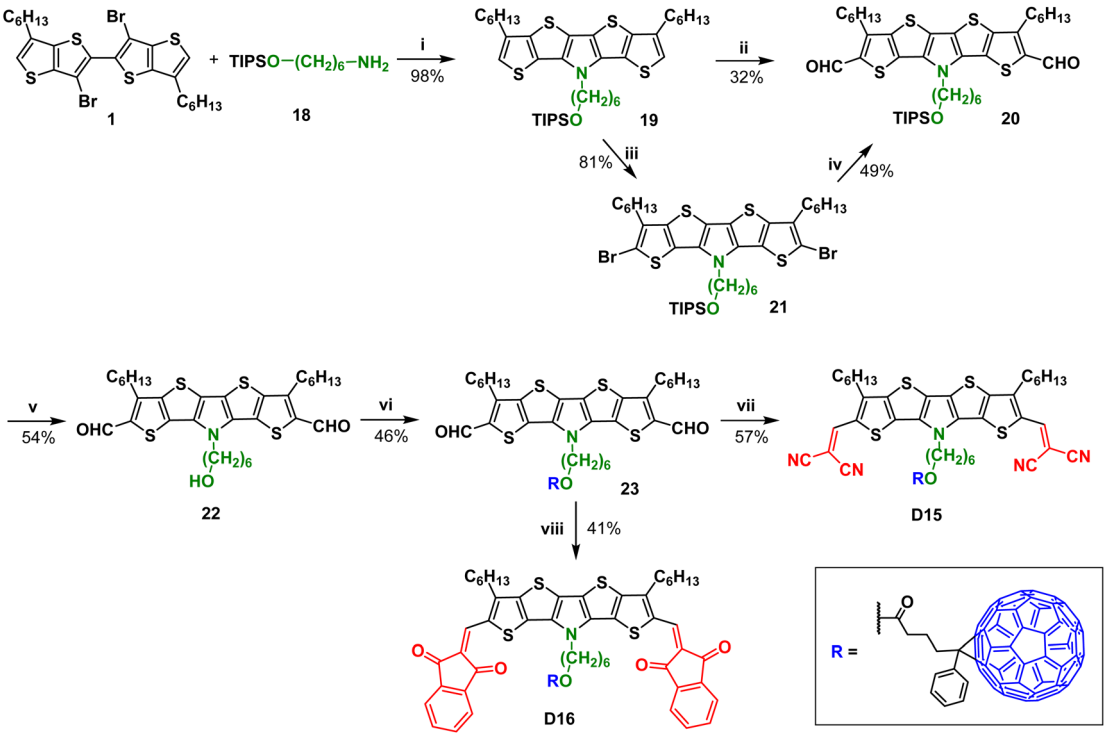

Scheme 6 Synthetic route to **D15** and **D16** with hexyl ester spacers: (i) $Pd(dba)_2$, dppf, NaO^tBu, toluene, 110 °C, 24 h; (ii) *n*-BuLi, *N*-Fpip, THF, −78 °C to rt, 24 h; (iii) $CHCl_3$, NBS, 0 °C–rt, 3 h; (iv) *n*-BuLi, *N*-Fpip, THF, −78 °C to rt, 24 h, (v) THF/HCl (30%) in 2 : 1 ratio, 70 °C, 5 h; (vi) PCBA, EDC·HCl, DMAP, CB/CS_2, 4 d, 40 °C; (vii) malononitrile, DCE, NH_4OAc, 80 °C, 6 d; (viii) Ind, DCE, piperidine, rt, 48 h.

intermediate D–A dyad **27** (92%). Typical Knoevenagel condensation of dialdehyde **27** gave targeted DCV-substituted **D17** (91%) and Ind-substituted **D18** (65%) (Scheme 7).

The structures of all novel *S,N*-heteroacenes **3**–**27** and dyads **D11**–**D18** were fully characterized by ^1H and ^{13}C-NMR spectroscopy and high-resolution mass spectrometry (HRMS). We additionally prepared and characterized reference derivatives **R11**–**R13** and **R15**–**R18**, which consisted of the identical ADA-core structure but lacked the pending fullerene $PC_{61}BA$ group. **R14** was not synthesized due to a different synthetic route to **D14**. Experimental and spectroscopic data are presented in the ESI.‡

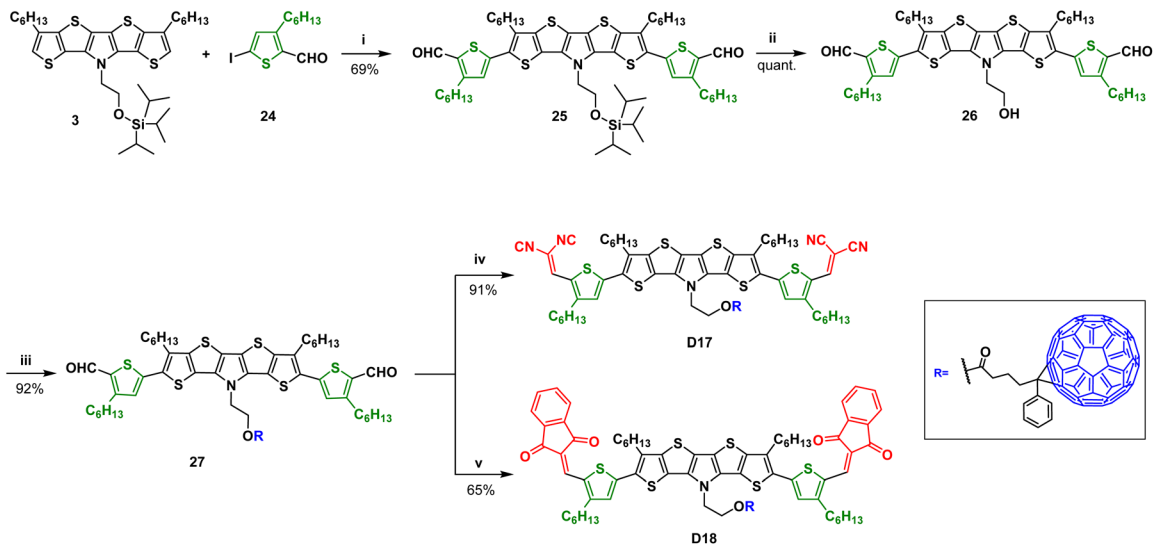

Scheme 7 Synthetic route to **D17** and **D18**: (i) $Pd(OAc)_2$, KOAc, DMF, 70–90 °C, 17 h; (ii) TBAF, THF, rt, 2.5 h; (iii) $PC_{61}BA$, DMAP, EDC·HCl, TEA, CB : CS_2 (2 : 1), 40 °C, 4 d; (iv) malononitrile, NH_4OAc, DCE, 80 °C, 15 h; (v) Ind, DCE, piperidine, rt, 21 h.

Thermal properties of D–A dyads D11–D18

Differential scanning calorimetry (DSC) and thermal gravimetric analysis (TGA) were used to determine the thermal properties of dyads **D11–D18** which are important for evaluating processing temperatures and long-term stability of photovoltaic devices. Typically, DSC traces of our previous DTP-based D–A dyads (**D1–D3**) in the first heating thermogram revealed endothermic peaks in the range of 100–130 °C which we assigned to glass transition temperatures T_g due to the mainly amorphous character of these dyads. Besides shallow exotherms at higher temperatures in the second DSC heating which arise from the movable pending fullerene ester side chains and reflect cold crystallization, typically no melting was identified.[12,21] In this respect, the investigation of novel SN5′-based dyads **D11–D18** partly revealed very shallow DSC traces, and therefore, T_gs were very difficult to identify. In contrast to the reference DTP-based dyads, various SN5′-dyads showed clear melting points T_m at higher temperatures which mainly were in accordance with the data from melting point apparatus (Table 1 and Fig. S8–S10, ESI‡).

Dyads **D11** and **D14** revealed small and broad endothermic peaks in the range of 180–200 °C which we assign to melting, whereby **D14** melted at a slightly lower temperature than **D11** due to the branching of the side chains in the SN5′ block. DSC traces of Ind-substituted **D12** and **D13** were very shallow and no phase transitions could be extracted indicating a fully amorphous character of these molecules. DSC traces of dyads **D15–D18** revealed endothermic peaks between 277 °C and 310 °C which most probably point to melting with subsequent decomposition (due to the lack of a corresponding peak in the back scan) arising from structural variations. **D17** and **D18** showed exothermic peaks between 215 °C and 240 °C which we assign to cold crystallization of the donor moiety. Shallow exotherms at around 260 °C in all heating scans of the dyads arise from the movable pending fullerene ester side chains and as well reflect cold crystallization.[21]

Most of the novel dyads exhibited good thermal stabilities with decomposition ranges above 355 °C (@5% mass loss) as measured by TGA. Compared to the DCV-based dyads (T_d = 388–398 °C), the Ind-substituted dyads degraded at somewhat lower temperatures of T_d = 358–365 °C, which we ascribe to the lower stability of the Ind-acceptors (Table 1 and Fig. S11–S13, ESI‡).

Table 1 Thermal properties of dyads **D11–D18**

Dyad	ADA acceptor	T_g (DSC)[a] [°C]	T_m (DSC)	T_d (TGA)[b] [°C]
D11	DCV	n.d.	185–200	398 (78%)
D12	Ind	n.d.	n.d.	363 (71%)
D13	Cl_2-Ind	n.d.	n.d.	358 (70%)
D14	DCV	n.d.	178–188	388 (75%)
D15	DCV	n.d.	295–310	388 (75%)
D16	Ind	n.d.	287–301	358 (66%)
D17	DCV	(125–145)	291–308	398 (72%)
D18	Ind	n.d.	277–302	363 (66%)

[a] Endothermic phase transition range. [b] Degradation temperature (5% mass loss) and mass at 800 °C in percent (n.d. = not clearly detectable).

Optical properties of D–A dyads D11–D18 and their reference derivatives

The optical properties of **D11–D18** and their references (**R11–R13** and **R15–R18**) without the pendant fullerene unit were investigated by UV-vis and fluorescence spectroscopy in dichloromethane (DCM). All DCV-terminated dyads showed decent solubility in DCM ranging from 2.6 mg mL^{-1} for **D15** to 27.6 mg mL^{-1} for **D14**, which in the latter case clearly showed the impact of the branched side chains on solubility. Additionally, the absorption spectra of thin films, which were prepared by spin-coating of chloroform (CF) solutions onto glass slides, were investigated. Full data are summarized in Table 2.

As an example, the absorption and emission spectra of D–A dyad **D11** (red curve) in comparison to references **R11** (blue) and $PC_{61}BM$ (black) are shown in Fig. S5 (ESI‡). Typically, the absorption profiles of the D–A dyads reflect a superimposition of the spectra of the individual subunits. Thus, in the spectrum of **D11**, the strong high energy absorption band around 260 nm and the smaller one at 329 nm can be assigned to the pendant fullerene group well coinciding with the spectrum of fullerene $PC_{61}BM$, whereby it is missing for reference **R11**. The second strong and vibronically split band in the visible range at 565 nm corresponds to a π–π* transition with charge-transfer (CT) character of the heteroacene backbone in accordance with **R11** (568 nm) and the corresponding *N*-alkylated SN5′-derivatives (567 nm).[14] The emission maximum of **D11** appeared at lower energies at 595 nm and also very close to that of reference **R11** (601 nm).

The solution (left) and normalized film absorption (right) spectra of **D11** (red curve), **D12** (blue), **D13** (purple), **D17** (green), and **D18** (black) are shown in Fig. 2. The corresponding emission spectra are plotted in Fig. S6 (ESI‡). The influence of the increasing strength of the terminal acceptor groups in the ADA SN5′ unit becomes obvious in the absorption spectra of the series **D11–D13**. Here, the π–π* transition of the backbone is gradually bathochromically shifted with increasing acceptor strength from 565 nm for DCV-**D11** to 623 nm for Ind-**D12** and to 646 nm for Cl_2-Ind **D13**. Their molar extinction coefficients were well above 100 000 M^{-1} cm^{-1} for the dyads and references **R11–R13**, which expectedly showed only marginal deviations in the absorption maxima compared to those of the dyads. The emission maxima appeared at lower energies in the range of 595–688 nm for both series (Fig. S6, ESI‡). The optical gaps were calculated from the absorption onset of the longest wavelength absorption at the low energy side and analogously became gradually smaller from E_g = 2.07 eV to 1.80 eV for **D11** to **D13** due to the continuous lowering of the energy level of the lowest unoccupied molecular orbital (LUMO) (*vide infra*) with increasing

Table 2 Optical data of SN5′-dyads **D11–D18** and their references **R11–R13** and **R15–18**

SN5′	λ_{max}^{sol} [nm]	E [L mol^{-1} cm^{-1}]	λ_{on}^{sol} [nm]	E_g^{sol} [eV]	Stokes shift [cm^{-1}]	λ_{max}^{em} [nm]	λ_{max}^{film} [nm]	λ_{on}^{film} [nm]	E_g^{film} [eV]
D11	**260**, 565	103 292	599	2.07	892	595	333, 550, **591**	644	1.93
R11	568	115 547	603	2.06	967	601	554, **604**	654	1.90
D12	**258**, 623	125 735	664	1.87	968	663	332, 615, **650**	725	1.71
R12	627	142 839	670	1.85	934	666	**608**, 648	712	1.74
D13	**259**, 646	104 165	690	1.80	945	688	336, 630, **674**	742	1.67
R13	651	134 952	695	1.78	826	688	524, **621**, 671	735	1.69
D14	**260**, 565	97 556	600	2.07	892	595	333, 551, **585**	635	1.95
D15	**260**, 570	111 322	605	2.05	905	601	333, 557, **593**	649	1.91
R15	568	123 963	604	2.05	967	601	**549**, 591	653	1.90
D16	**259**, 627	128 473	669	1.85	979	668	333, **603**, 650	724	1.71
R16	625	148 028	669	1.85	985	666	**600**, 656	724	1.71
D17	**260**, 600	77 202	673	1.84	2542	708	333, **620**	738	1.68
R17	606	94 844	680	1.82	2516	715	392, 607, **641**	738	1.68
D18	**260**, 628	53 235	710	1.75	2679	755	328, 406, **646**	777	1.59
R18	638	80 420	721	1.72	2704	771	420, 647, **694**	812	1.53
$PC_{61}BM$	**261**, 328	121 798	401	3.09	—	—	336	570	2.18

Spectra of dyads **D11–D18**, references **R11–R13**, **R15–18** and $PC_{61}BM$ were recorded in DCM, global maxima are in bold font. Molar extinction coefficients are given for the longest wavelength absorption with CT contribution. The optical energy gap was calculated with $1240/\lambda_{onset}$, and Stokes shifts were calculated by subtracting the emission maximum from the absorption maximum in wavenumbers.

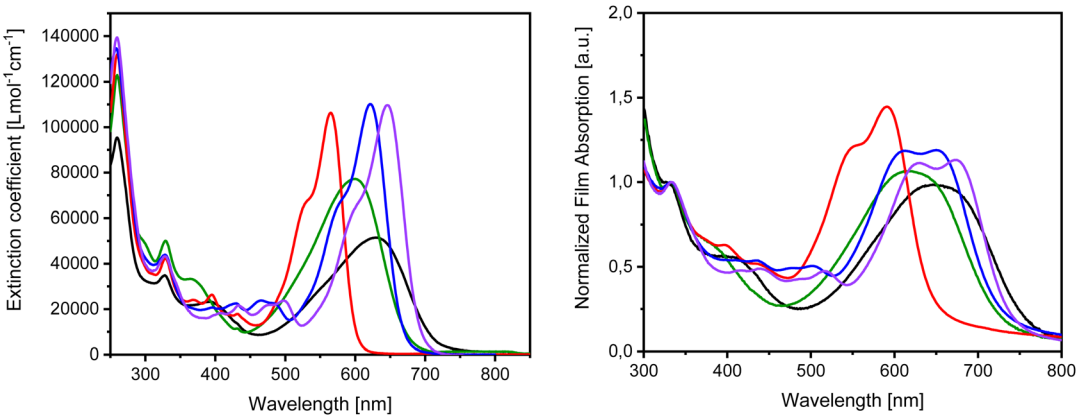

Fig. 2 Solution absorption spectra of **D11** (red), **D12** (blue), **D13** (purple), **D17** (green), and **D18** (black) recorded in DCM solution (left). Normalized thin film absorption spectra spin-coated from chloroform solution and normalized to the fullerene band at around 333 nm (right).

acceptor strength. Again, the references showed only very small differences compared to the dyads.

Expectedly, the influence of the branched EtHex side chains at the β-positions of the SN5′-core in DCV-**D14** on the optical data is only marginal and is in accordance with hexyl-substituted DCV-based **D11**. Also, the enlargement of the insulating linker between the SN5′-donor and the fullerene acceptor unit from an ethyl to a hexyl ester chain in DCV-**D15** and Ind-**D16** as expected did not largely influence the optical properties of the corresponding conjugated π-systems. In comparison to DCV-**D11** and Ind-**D12**, the absorption and emission maxima were only slightly shifted.

In contrast, the elongation of the conjugated donor block by two additional 3-hexylthiophene units in DCV-based **D17** and Ind-based **D18** led to bathochromically shifted absorptions and in particular emission maxima compared to those of the preceding **D11** and **D12**. This structurally caused effect is distinctly larger for the pair DCV-**D11**/**D17** ($\Delta\lambda$ = 35 nm) than for Ind-**D12**/**D18** ($\Delta\lambda$ = 5 nm). Due to the higher degree of rotational freedom of the additional thiophene units in the donor core, broader and less structured absorption bands were noted. The same structural reason led to much larger Stokes shifts (>2500 cm^{-1}) for the more flexible **D17** and **D18** than for **D11** and **D12** (≤985 cm^{-1}) comprising much stiffer backbones.

The absorptions of the D–A systems **D11–D18** and the corresponding references in the solid state were investigated in thin films, which were prepared by spin-coating chloroform (CF) solutions onto glass slides. In general, the film absorption spectra showed the same trends as the solution spectra, whereby the bands are broadened due to the increased intermolecular interactions and typically red-shifted by 20–40 nm. In this respect, the maxima of the longest wavelength band appeared in the region of 585–694 nm depending on the type of acceptor in the ADA donor backbone. The main fullerene band below 300 nm was cut off due to the absorption of the glass slide, and therefore, only the smaller band was visible in

a small range (332–336 nm) and expectedly was not dependent on the donor block structure. As a consequence, the optical gaps were diminished to E_g = 1.95–1.59 eV for the films compared to the solution data. As before, the values for the references only deviate slightly by few nano-meters.

When summarizing the optical properties of the series at a glance, the largest influence of structure on the absorption and emission behavior came from the variation of the terminal acceptor groups and the elongation of the conjugated π-system, both in the ADA core.

Electrochemical properties of D–A dyads D11–D18 and their reference derivatives

The redox properties of D–A dyads **D11–D18** and their references were investigated by cyclic voltammetry (CV) and differential pulse voltammetry (DPV) in DCM solution with tetrabutylammonium hexafluorophosphate ($TBAPF_6$, 0.1 M) as supporting electrolyte, and potentials were referenced against the ferrocene/ferricenium couple (Fc/Fc^+), whereby the energy level of Fc/Fc^+ was set to −5.1 eV against vacuum.[22] HOMO and LUMO energies were calculated from the onset values of the first oxidation and reduction wave, respectively, which were graphically determined. The electrochemical energy gap was calculated as the difference between the HOMO and LUMO energy levels. The summarized data are compiled in Table 3.

The CV and DPV profiles of various dyads are quite complex comprising numerous oxidation and reduction waves which typically reflect the superimposition of the redox processes of the D and A subunits (Fig. S7, ESI‡) as it was found for the previously published dyads **D1–D4**[12] and in accordance with the optical investigation (*vide supra*). The assignment of the redox waves to individual molecular units was undertaken by analysis and comparison to the electrochemical responses of the corresponding reference derivatives and $PC_{61}BM$.

First, we discuss the series of DCV-terminated dyads **D11**, **D14**, **D15**, and **D17**. In the cathodic region, we typically identified up to five separated (quasi) reversible waves due to the multiple reductions of the electron-accepting fullerene and the DCV-termini of the SN5′ core unit. By comparing the half-wave potentials of **D11** with those of references **R11** and $PC_{61}BM$, we assign the 1st ($E_{1/2}^{Red1}$ = −1.09 V), the 3rd ($E_{1/2}^{Red3}$ = −1.45 V), and the 5th ($E_{1/2}^{Red5}$ = −1.99 V) reduction wave to the pendant fullerene concomitant with the formation of radical anions up to trianions. The 2nd ($E_{1/2}^{Red2}$ = −1.29 V) and 4th ($E_{1/2}^{Red4}$ = −1.62 V) waves can be assigned to the reduction of the terminal DCV units of the ADA donor system, which are reduced to a radical anion each (Fig. 3). The corresponding peak potentials for the other DCV-dyads **D14**, **D15**, and **D17** vary only moderately; however, sometimes the reduction waves are not well resolved or overlaid.

In the anodic region, two oxidation processes were noted for **D11** representing the formation of stable radical cations ($E_{1/2}^{Ox1}$ = 0.84 V), which are delocalized on the SN5′ donor block,[14] and the oxidation of the $PC_{61}BM$ unit ($E_{1/2}^{Ox2}$ = 1.11 V). The first value coincides well with the oxidation of **R11** ($E_{1/2}^{Ox}$ = 0.77 V) and the second agrees well with that of $PC_{61}BM$ ($E_{1/2}^{Ox}$ = 1.09 V) which was measured independently for comparison and of course is missing in the CV/DPV of **R11** (Fig. 3).[23] The energy levels of the frontier orbitals were determined to −5.87 eV (HOMO) and −4.08 eV (LUMO), which correspond well to the HOMO of **R11** and the LUMO of $PC_{61}BM$, respectively, leading to an electrochemical energy gap of 1.79 eV.

DCV-based dyads **D14** and **D15** behaved quite similarly with only marginal differences, whereby in the case of **D17**, two overlapped oxidation peaks at much lower potentials ($E_{1/2}^{Ox1}$ = 0.35 V and $E_{1/2}^{Ox2}$ = 0.44 V) than those of the other dyads were noted due to the extended conjugated π-system in the ADA donor part. As we have already seen for similar ADA SN5′

Table 3 Electrochemical data of SN5′-dyads **D11–D18** and their references **R11–R13** and **R15–18**. CVs and DPVs were measured in dichloromethane ($c = 10^{-3}$ M), with $TBAPF_6$ as supporting electrolyte (0.1 M) at a scan speed of 100 mV s^{-1} at r.t. Potentials are given *vs.* the internal standard ferrocene/ferricenium (Fc/Fc^+)

SN5′	Acc (ADA)	$E_{1/2}^{Ox}$ [a] [V]	$E_{1/2}^{Red}$ [a] [V]	HOMO[b] [eV]	LUMO[b] [eV]	E_g^{CV} [c] [eV]
D11	DCV	0.84, 1.11	−1.09, −1.29, −1.45, −1.62, −1.99	−5.87	−4.08	1.79
R11	DCV	0.77	−1.32, −1.66	−5.83	−3.87	1.96
D12	Ind	0.54, 0.68, 1.15	−1.12, −1.31, −1.51, −1.69, −1.99	−5.55	−4.05	1.50
R12	Ind	0.60, 0.87[e], 1.15[e]	−1.21, −1.52	−5.63	−3.94	1.69
D13	Cl_2-Ind	0.74, 1.28	−1.04, −1.28, −1.38[e], −1.60, −1.92	−5.77	−4.09	1.68
R13	Cl_2-Ind	0.61, 0.88[e]	−1.13, −1.34[e], −1.53	−5.62	−3.99	1.63
D14	DCV	0.86, 1.14	−1.05, −1.31[e], −1.40, −1.60, −1.95	−5.93	−4.05	1.88
D15	DCV	0.78, 1.10	−1.19, (n.r.)[d], −1.55, −1.72[e], −2.07	−5.83	−4.01	1.82
R15	DCV	0.75	−1.37, −1.80	−5.53	−3.91	1.62
D16	Ind	0.46, 0.67, 1.10	−1.14, −1.32[e], −1.48, −1.54[e], −2.02	−5.49	−4.02	1.47
R16	Ind	0.44, 0.66, 1.15	−1.34, −1.51 [e], −1.59 [e],	−5.48	−3.83	1.65
D17	DCV	0.35, 0.90, 1.09, 0.44	−1.11, −1.39[e], −1.47, (n.r.)[d], −2.02	−5.37	−4.06	1.31
R17	DCV	0.21, 0.85, 0.36	−1.50[e], −1.67	−5.27	−3.7	1.57
D18	Ind	0.07, 0.75, 1.06, 0.24	−1.22, (n.r.)[d], −1.53, −1.72[e], −2.09	−5.11	−3.96	1.15
R18	Ind	0.06, 0.81, 0.24	−1.36, −1.44	−5.14	−3.55	1.59
$PC_{61}BM$	$PC_{61}BM$	1.09	−1.17, −1.55, −2.06	−6.09	−3.99	2.10

[a] Determined from differential pulse voltammetry (DPV). [b] Calculated from the onset values of the first oxidation and reduction waves by setting the ferrocene HOMO energy to −5.1 eV *vs.* vacuum. (E_{HOMO} = −5.1 eV − $E_{on,\ Ox}$; E_{LUMO} = −5.1 eV − $E_{on,\ Red}$). [c] $E_g = E_{LUMO} - E_{HOMO}$. [d] n.r. not resolved. [e] Shoulder, overlaid.

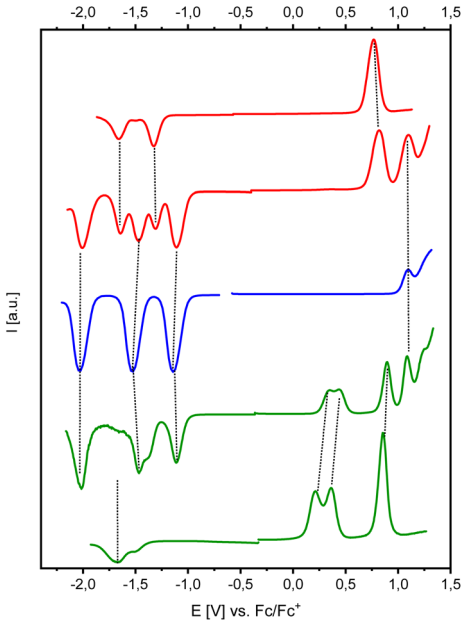

Fig. 3 DPV of reference **R11** (red curve, top), dyad **D11** (red, second top), reference $PC_{61}BM$ (blue, middle), dyad **D17** (green, second bottom) and reference **R17** (green, bottom), measured in DCM solution, using $TBAPF_6$ as a conducting salt, referenced against Fc/Fc^+ as an internal standard, scan speed 0.1 V s^{-1} at r.t.

derivatives, chemical equilibria are involved in the oxidation processes.[14] Therefore, the two superimposed waves correspond to the formation of equilibrated monomeric and dimeric radical cations in accordance with the transfer of one electron in total. The subsequent third wave at $E_{1/2}^{Ox3}$ = 0.90 V correlates to the transfer of one electron and represents the formation of dications delocalized over the donor unit. As before, the fourth oxidation process ($E_{1/2}^{Ox4}$ = 1.09 V) is assigned to the one-electron oxidation of the pendant $PC_{61}BM$ unit (Fig. 3). Due to the lower first oxidation potential, the HOMO of **D17** is substantially stabilized and the energy increased to −5.37 eV, which resulted in a smaller energy gap of 1.31 eV. Reference **R17** electrochemically behaved equally with the exception that the $PC_{61}BM$ oxidation peak is missing.

The series of **D12** (**D13**), **D16**, and **D18** and their corresponding references **R12** (**R13**), **R16**, and **R18** bear stronger electron-withdrawing Ind (or CI_2-Ind) groups in the ADA donor core unit. Nevertheless, their first oxidation potentials were negatively shifted with respect to the DCV derivatives. This phenomenon was already noted and explained for alkylated Ind-substituted SN5′-systems by the contribution of intramolecular noncovalent S···O interactions of the carbonyl group of each Ind-acceptor moiety with the sulfur of the corresponding terminal thiophene unit in the SN5′ core, leading to planarization and an elongated conjugated π-system.[14] In contrast to the DCV derivatives, the second oxidation peak belongs to the monomer–dimer equilibrium and the third oxidation is an overlay of the formation of the $PC_{61}BM$ radical cation and the formation of the dication of the ADA donor system.

In the reductive potential region, the redox behaviour of the Ind-series is very similar to that of the DCV derivatives. The assignment of the various reduction waves is identical and the reduction of the Ind-acceptor subunits in the ADA system for the sequential formation of radical anions occurs at similar potentials to those of the DCV groups.

To shortly summarize the redox properties of the series, the complex CV/DPVs are dominated by the superposition of the individual redox response of the SN5′ donor and the $PC_{61}BA$ subunit. The largest influence of structure on the redox behaviour came from the elongation of the conjugated π-system by two additional thiophene units in the ADA-core, leading to well-decreased oxidation potentials.

Photovoltaic characterization of dyads D11–D18 in single-material organic solar cells

The synthesized D–A dyads **D11–D18** were implemented in single-material organic solar cells (SMOSC) as sole materials in the active layer. The general solar cell device structure was glass/ITO/PEDOT:PSS/**dyad**/LiF/Al which was prepared under ambient conditions by spin-coating the solutions of the respective materials followed by individual optimization. Processing parameters such as processing solvent, temperature, spin speed, and post-treatment methods such as thermal annealing (TA) or solvent vapor annealing (SVA) were varied. Table 4 presents the summary of devices with the highest achieved PCE. The device optimization of each D–A dyad is presented in the ESI (Tables S1–S9‡). DCV-based dyad **D11**

Table 4 Photovoltaic parameters of SN5′-dyads **D11–D18** in optimized single-material organic solar cells (SMOSC)

DA dyad	V [rpm]	SVA	V_{OC} (V)	J_{SC} (mA cm^{-2})	FF	PCE (%)
D11[a]	2000	30 s THF	0.68 ± 0.03 (0.70)	0.32 ± 0.02 (0.36)	0.26 ± 0.00 (0.27)	0.06 ± 0.00 (0.07)
D12[c]	3000	10 s CS_2	0.79 ± 0.01 (0.80)	1.32 ± 0.03 (1.35)	0.24 ± 0.00 (0.24)	0.25 ± 0.01 (0.26)
D13[b]	3000	—	0.68 ± 0.05 (0.75)	0.19 ± 0.00 (0.20)	0.28 ± 0.01 (0.29)	0.04 ± 0.00 (0.04)
D14[d]	2000	30s CS_2	0.67 ± 0.12 (0.78)	0.13 ± 0.01 (0.14)	0.25 ± 0.01 (0.26)	0.02 ± 0.00 (0.03)
D15[d]	1000	—	0.39 ± 0.14 (0.60)	0.26 ± 0.01 (0.28)	0.27 ± 0.01 (0.28)	0.03 ± 0.01 (0.04)
D16[d]	2000	20 s CS_2	1.04 ± 0.00 (1.04)	7.44 ± 0.49 (7.95)	0.34 ± 0.01 (0.35)	2.63 ± 0.21 (2.83)
D17[d]	2000	—	0.48 ± 0.07 (0.58)	0.02 ± 0.01 (0.03)	0.13 ± 0.03 (0.18)	0.00
D18[d]	3000	20s CS_2	0.68 ± 0.01 (0.69)	3.11 ± 0.10 (3.66)	0.34 ± 0.01 (0.35)	0.81 ± 0.04 (0.86)

Average value of four cells ± standard deviation (maximum); cell architecture: glass/ITO/PEDOT:PSS/dyad/LiF/Al; processed by spin-coating. [a] CB (80 °C), 15 mg mL^{-1}. [b] CF (50 °C), 15 mg mL^{-1}. [c] CB (rt), 15 mg mL^{-1}. [d] CF (rt), 15 mg mL^{-1}.

showed a very low PCE (0.07%) mainly arising from low photocurrent density (J_{SC} = 0.36 mA cm^{-2}) and fill factor (FF = 0.27). We attribute this finding to the moderate solubility of the dyad which had to be spin-coated from chlorobenzene (CB) at 80 °C. Despite the well increased solubility and better film quality of EtHex-dyad **D14**, unfortunately, no positive impact on PCE (0.02%) was noted. We rationalize this result as due to the steric hindrance of the EtHex-side chains, which hinder the packing due to the DCV groups and consequently perturb the molecular arrangement and reduce intermolecular interactions in the solid film.[24] Neither the elongation of the flexible linker in DCV-dyad **D15** nor the elongated π-system in **D17** resulted in PCEs larger than 0.04% reinforcing the abovementioned assumption. As before, unusually low $J_{SC} \leq 0.28$ mA cm^{-2} and FFs ≤ 0.28 were found.

These results clearly show that the replacement of the DTP core unit in DCV-based dyads **D1–D3**, which showed PCEs of up to 4.2%, with the SN5′ core in dyads **D11**, **D14**, **D15**, and **D17** turned out to be rather counterproductive with respect to photovoltaic performance in SMOSCs and most probably is down to the unfavorable morphology of the films.

When the structurally related Ind-based dyads **D12** (**D13**), **D16**, and **D18** were compared to the DCV-based dyads, the elongation of the spacer from ethyl ester in **D12** to hexyl ester in **D16** led to an increase of the average PCE from 0.25% to 2.63%. The corresponding current–voltage (*J*–*V*) curve of the cell with the highest efficiency is shown in Fig. 4, which turned out to be the best average value in the whole series, whereby the elongation of the π-system in **D18** resulted in a smaller increase of PCE to 0.81%. In comparison with the DCV-based dyads, which showed severe voltage losses, this substantial PCE improvement mainly arises from higher V_{OC}s (≤1.04 V) and J_{SC}s (≤7.95 mA cm^{-2}). Thus, the longer flexible linker in **D16** and the Ind-acceptor groups obviously allow for more favorable self-organization of the molecules in the solid state. Nevertheless, an *N*-alkylated Ind-SN5′ derivative, which is directly comparable to **R16**, as the donor component in biphasic BHJSCs with $PC_{61}BM$ as the acceptor in a ratio of 1 : 1.25 achieved a distinctly higher PCE of 5.5%[14] than **D16**, owing to the increased photovoltaic parameters, in particular with respect to J_{sc} and FF.

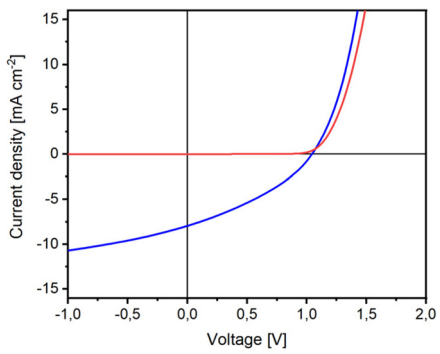

Fig. 4 *J*–*V* curves of the single-material solar cell with dyad **D16** in the dark (red curve) and under AM1.5G illumination (blue).

Conclusion

In summary, we have presented multi-step syntheses and characterization of novel donor–acceptor dyads **D11–D18** in good overall yields. The synthetic design comprised functionalized S,N-heteropentacenes SN5′ as central donor units and fullerenic $PC_{61}BA$ units as acceptors, which were appended *via* a flexible alkyl ester linker. The structural motifs were varied systematically such as the variation of acceptor moieties (DCV, Ind, and Cl_2-Ind) in the ADA donor unit, the variation of spacer length (ethyl and hexyl ester), and the elongation of the conjugated SN5′ system using additional thiophene units. The influence of the structural variations on their molecular and physical properties was investigated which generally showed the superposition of the electronic behavior of the specific donor and $PC_{61}BA$-fullerene unit. In this connection, the largest influence of structure on optical and redox properties came from the elongation of the conjugated π-system and the variation of the terminal acceptor groups, both in the ADA core unit of the dyads. The specific absorption profiles and energetic position of the frontier orbitals allowed for the application of the D–A dyads in solution-processed SMOSCs. The investigation of their photovoltaic behavior as a sole photoactive component resulted in a rather moderate performance of the implemented dyads most probably due to problems in film formation and subsequent low ordering in the photoactive layer. However, the best result in the series with an acceptable PCE of 2.8% was obtained from dyad **D16**, in which the longer flexible hexyl ester linker and the Ind-acceptor groups obviously allowed for more favorable self-organization of the molecules in the solid state. The overall elaborated qualitative structure–property–device performance relationship in our series of eight novel D–A dyads **D11–D18** will be helpful to further develop the rational design of improved molecular materials for SMOSCs.

Conflicts of interest

The authors declare no conflict of interest.

Acknowledgements

We thank Dr Markus Wunderlin, service center mass spectrometry, University of Ulm, for measuring a large number of mass spectra. We as well thank K. Fedke, Inorganic Chemistry II, University of Ulm, for measuring TGAs.

References

1 (*a*) Z. Cai, M. A. Awais, N. Zhang and L. Yu, Exploration of Syntheses and Functions of Higher Ladder-type π-Conjugated Heteroacenes, *Chem*, 2018, **4**, 1–33; (*b*) E. Brier, C. Wetzel, M. Bauer, M. Wunderlin and

P. Bäuerle, *S*,*N*-Heteroacenes Up to a Tridecamer, *Chem. Mater.*, 2019, **31**, 7007–7023.

2 C. Bulumulla, R. Gunawardhana, P. L. Gamage, J. T. Miller, R. N. Kularatne, M. C. Biewer and M. C. Stefan, Pyrrole-containing semiconducting materials: synthesis and applications in organic photovoltaics and organic field-effect transistors, *ACS Appl. Mater. Interfaces*, 2020, **12**, 32209–32232.

3 N. Arora, C. Wetzel, M. I. Dar, A. Mishra, P. Yadav, C. Steck, S. M. Zakeeruddin, P. Bäuerle and M. Grätzel, Donor-Acceptor-Type *S*,*N*-Heteroacene-Based Hole-Transporting Materials for Efficient Perovskite Solar Cells, *ACS Appl. Mater. Interfaces*, 2017, **9**, 44423–44428.

4 A. Mishra, D. Popovic, A. Vogt, H. Kast, T. Leitner, K. Walzer, M. Pfeiffer, E. Mena-Osteritz and P. Bäuerle, ADA-type *S*,*N*-Heteropentacenes: Next-Generation Molecular Donor Materials for Efficient Vacuum-Processed Organic Solar Cells, *Adv. Mater.*, 2014, **26**, 7217–7223.

5 (*a*) X. Chen, H. Liu, L. Xia, T. Hayat, A. Alsaedi and Z. Tan, A pentacyclic *S*,*N*-heteroacene based electron acceptor with strong near-infrared absorption for efficient organic solar cells, *Chem. Commun.*, 2019, **55**, 7057–7060; (*b*) T. Leitner, A. Vogt, D. Popović, E. Mena-Osteritz, K. Walzer, M. Pfeiffer and P. Bäuerle, Influence of alkyl chain length in *S*,*N*-heteropentacenes on the performance of organic solar cells, *Mater. Chem. Front.*, 2018, **2**, 959–968.

6 Y. Cui, Y. Xu, H. Yao, P. Bi, L. Hong, J. Zhang, Y. Zu, T. Zhang, J. Qin, J. Ren, Z. Chen, C. He, X. Hao, Z. Wie and J. Hou, Single-junction organic photovoltaic cell with 19% efficiency, *Adv. Mater.*, 2021, **33**, 2102420.

7 (*a*) J. Roncali and I. Grosu, The dawn of single material organic solar cells, *Adv. Sci.*, 2019, **6**, 1801026; (*b*) J. Roncali, Single-Material Organic Solar Cells Based on Small Molecule Homojunctions: An Outdated Concept or a New Challenge for the Chemistry and Physics of Organic Photovoltaics, *Adv. Energy Mater.*, 2021, **11**, 2102987.

8 O. Almora, D. Baran, G. C. Bazan, C. Berger, C. I. Cabrera, K. R. Catchpole, S. Erten-Ela, F. Guo, J. Hauch, A. W. Y. Ho-Baillie, T. J. Jacobsson, R. A. J. Janssen, T. Kirchartz, N. Kopidakis, Y. Li, M. A. Loi, R. R. Lunt, X. Mathew, M. D. McGehee, J. Min, D. B. Mitzi, M. K. Nazeeruddin, J. Nelson, A. F. Nogueira, U. W. Paetzold, N.-G. Park, B. P. Rand, U. Rau, H. J. Snaith, E. Unger, L. Vaillant-Roca, H.-L. Yip and C. J. Brabec, Device Performance of Emerging Photovoltaic Materials, *Adv. Energy Mater.*, 2021, **11**, 2102526.

9 Y. He, N. Li, T. Heumüller, J. Wortmann, B. Hanisch, A. Aubele, S. Lucas, G. Feng, X. Jiang, W. Li, P. Bäuerle and C. J. Brabec, Industrial viability of single-component organic solar cells, *Joule*, 2022, **6**, 1160–1170.

10 X. Yang, Y. Wu, Y. Gao, J. Guo, W. Wang and J. Min, Over 13% Efficient Single-Component Organic Solar Cells Enabled by Adjusting the Conjugated-Length of Intermediate PBDB-T Block, *Adv. Funct. Mater.*, 2022, **31**, 2208412.

11 S. Liang, C. Xiao, C. Xie, B. Liu, H. Fang and W. Li, 13% Single-Component Organic Solar Cells based on Double-Cable Conjugated Polymers with Pendant Y-Series Acceptors, *Adv. Mater.*, 2023, e2300629.

12 (*a*) S. Lucas, J. Kammerer, M. Pfannmöller, R. R. Schröder, Y. He, N. Li, C. J. Brabec, T. Leydecker, P. Samorì, T. Marzalek, W. Pisula, E. Mena-Osteritz and P. Bäuerle, Molecular Donor-Acceptor Dyads for Efficient Single-Material Organic Solar Cells, *RRL Sol.*, 2021, **5**, 2000653; (*b*) A. Aubele, Y. He, T. Kraus, N. Li, E. Mena-Osteritz, P. Weitz, T. Heumüller, K. Zhang, C. J. Brabec and P. Bäuerle, Molecular Oligothiophene-Fullerene Dyad Reaching Over 5% Efficiency in Single-Material Organic Solar Cells, *Adv. Mater.*, 2022, **34**, 202103573.

13 Dyads **1–4** have already been published [see ref. 12] and structurally related dyads **5–10** will be released in a separate forthcoming paper (A. Aubele, T. Kraus, S. Schmid, E. Mena-Osteritz and P. Bäuerle, *Chem. – Eur. J.* under review).

14 T. Kraus, S. Lucas, P. Wolff, A. Aubele, E. Mena-Osteritz and P. Bäuerle, Advanced Acceptor-Substituted *S*,*N*-Heteropentacenes for Application in Organic Solar Cells, *Chem. – Eur. J.*, 2021, **27**, 10913–10924.

15 (*a*) S. B. Dkhil, M. Pfannmöller, I. Ata, D. Duché, M. Gaceur, T. Koganezawa, N. Yoshimoto, J.-J. Simon, L. Escoubas, C. Videlot-Ackermann, O. Margeat, S. Bals, P. Bäuerle and J. Ackermann, Time evolution studies of dithieno[3,2-*b*: 2′,3′-*d*]pyrrole-based ADA oligothiophene bulk-heterojunctions during solvent vapor annealing towards optimization of photocurrent generation, *J. Mater. Chem. A*, 2017, **5**, 1005–1013; (*b*) I. Ata, S. B. Dkhil, M. Pfannmöller, S. Bals, D. Duché, J.-J. Simon, C. Videlot-Ackermann, O. Margeat, J. Ackermann and P. Bäuerle, The influence of branched alkyl side chains in ADA oligothiophenes on the photovoltaic performance and morphology of solution-processed bulk-heterojunction solar cells, *Org. Chem. Front.*, 2017, **4**, 1561–1573.

16 R. N. Zuckermann, E. J. Martin, D. C. Spellmeyer, G. B. Stauber, K. R. Shoemaker, J. M. Kerr, G. M. Figliozzi, D. A. Goff, M. A. Siam, R. J. Simon, S. Banville, E. Brown, L. Wang, L. Richter and W. Moos, Discovery of Nanomolar Ligands for 7-Transmembrane G-Protein-Coupled Receptors from a Diverse N-(Substituted)-glycine Peptoid Library, *J. Med. Chem.*, 1994, **37**, 2678–2685.

17 J.-H. Wan, W.-F. Fang, Z.-F. Li, X.-Q. Xiao, Z. Xu, Y. Deng, L.-H. Zhang, J.-X. Jiang, H.-Y. Qiu, L.-B. Wu and G.-Q. Lai, Novel Ladder π-Conjugated Materials-Sila-Pentathienoacenes: Synthesis, Structure, and Electronic Properties, *Chem. – Asian J.*, 2010, **5**, 2290–2296.

18 R. Graf, Umsetzung mit N-Carbonyl-sulfamidsäurechlorid, III. Umsetzung mit Olefinen und Aldehyden; über β-Lactame, *Liebigs Ann. Chem.*, 1963, **661**, 111–157.

19 A. B. Smith, N. Kanoh, H. Ishiyama, N. Minakawa, J. D. Rainier, R. A. Hartz, Y. S. Cho, H. Cui and W. H. Moser, Tremorgenic Indole Alkaloids. The Total Synthesis of (-)- Penitrem D, *J. Am. Chem. Soc.*, 2003, **125**, 8228–8237.

20 (*a*) N. Masuda, S. Tanba, A. Sugie, D. Monguchi, N. Koumura, K. Hara and A. Mori, Stepwise Construction

of Head-to-Tail-Type Oligothiophenes via Iterative Palladium-Catalyzed CH-Arylation and Halogen Exchange, *Org. Lett.*, 2009, **11**, 2297–2300; (*b*) J. Grolleau, P. Frère and F. Gohier, Clean and Efficient Iodination of Thiophene Derivatives, *Synthesis*, 2015, **47**, 3901–3906.

21 B. Hajduk, H. Bednarski, M. Domanski, B. Jarzabek and B. Trzebicka, Thermal Transitions on P3HT: $PC_{60}BM$ Films Based on Electrical Resistance Measurements, *Polymers*, 2020, **12**, 1458.

22 C. M. Cardona, W. Li, A. E. Kaifer, D. Stockdale and G. C. Bazan, Electrochemical Considerations for Determining Absolute Frontier Orbital Energy Levels of Conjugated Polymers for Solar Cell Applications, *Adv. Mater.*, 2011, **23**, 2367–2371.

23 Oxidation potentials of fullerenes are only scarcely found in the literature: $E_{Ox}^{1/2}$ = 1.26 V *vs.* Fc/Fc^{+} for C_{60}: Q. Xie, F. Arias and L. Echegoyen, Electrochemically-reversible, single-electron oxidation of C_{60} and C_{70}, *J. Am. Chem. Soc.*, 1993, **115**, 9818–9819.

24 R. Fitzner, C. Elschner, M. Weil, C. Uhrich, C. Körner, M. Riede, K. Leo, M. Pfeiffer, E. Reinold, E. Mena-Osteritz and P. Bäuerle, Interrelation between Crystal Packing and Small-Molecule Organic Solar Cell Performance, *Adv. Mater.*, 2012, **24**, 675–680.

